Chapter 10

Atmospheric Absorption

Juan Pardo[1,2]

pardo@isis.iem.csic.es

[1] CALTECH, Astronomy Department, Mail Stop 320-47 1200 E., California Blvd., Pasadena, CA 91125, USA

[2] Inst. Estructura de la Materia Dpto. Física Molecular Serrano, 121 Madrid, E-28006 Spain

This lecture is partially adapted from the IMISS1 course " Atmospheric Absorption" By Michel Guélin (sections 10.1 and 10.4.1). It also includes a description of the phase correction methods (sections 10.5.3 and 10.5.4) by Martina Wiedner. The author would like also to acknowledge the contributions of the following people: J. Cernicharo, E. Serabyn and S. Matsushita.

10.1 The physical and chemical structure of the Atmosphere

10.1.1 Constituents of the atmosphere

In order to study the effect of the atmosphere on the outcoming longwave radiation, it is convenient to subdivide it into a "clean dry" component, water vapor, and aerosols (water droplets, as well as ice crystals, salt grains & dust particles, which serve as condensation seeds for water).

Abundances Table 10.1 gives the standard composition of the "clean dry" air in the troposphere (i.e at altitudes ≤ 20 km). Except for CO_2, whose abundance at ground level may vary between day and night by up to a factor of 2, this composition is remarkably homogeneous and constant. Other trace components, most of which are unstable (SO_2, O_3, NO, CO, ...) have abundances (in volume) that never exceeds 10^{-5}.

The abundance of water is highly variable, but hardly exceeds 1% in mass, even locally. Most of the water in the air is in the form of vapor. Even inside the clouds, precipitation and turbulence insure that

Name	Molec. mass amu	Normal abund. (% in volume)	Name	Molec. mass amu	Normal abund. (% in volume)
N_2	28.013	78.084	He	4.003	0.0005
O_2	32.000	20.946	Kr	83.8	0.0001
Ar	39.948	0.934	CH_4	16.043	0.0002
CO_2	44.010	0.033^v	H_2	2.016	0.00005
Ne	20.183	0.0018	N_2O	44.013	0.00005

Table 10.1: Main constituents of the dry air in the troposphere.

the mass of water droplets per cm^{-3} seldom equals that of water vapor. In addition the water vapor mixing ratios above 15-20 km are under 10 ppmv making it just another trace gas there.

Overall picture of the atmospheric spectrum Despite the above facts, water, which has a large absorption cross section in the IR and a large specific heat of vaporization, ($L_w \sim 600$ cal/g), ozone, which has UV photodisociation bands playing a key role in the stratosphere, and carbon dioxide, which has large IR absorption cross sections, are the major actors of the thermal balance of the air.

Ozone and to much less extent molecular Oxygen are responsible for most of the absorption of the solar radiation in the UV, especially between 180 and 290 nm, thanks to these processes: $O_3 + h\nu(\lambda < 310\,nm) \rightarrow O_2(^1\Delta_g) + O(^1D)$ (Hartley band), $O_2(^3\Sigma_g^-) + h\nu(\lambda < 175nm) \rightarrow O(^3P) + O(^1D)$ (Schuman-Runge band), and $O_2(^3\Sigma_g^-) + h\nu(\lambda < 242nm) \rightarrow O(^3P) + O(^3P)$ (Herzberg band),

In the visible, the air is fairly transparent except for scattering by aerosols, mostly water droplets, ice crystals and dust particles. In the infrared, H_2O, CO_2 (around 15 μm) and O_3 (around 10μm) are very efficient absorbers of the solar and ground radiation, to the extent that they prevent ground-based observations in large regions of the electromagnetic spectrum.

By clear weather, the atmospheric absorption at millimeter and submillimeter wavelengths is dominated by rotational and fine structure lines of molecules in their ground electronic and low vibrational states.

The strongest molecular rotational resonances appear in polar molecules (H_2O and O_3 being the most important of such molecules in the atmosphere) and are of the type E1 (electric dipole transitions). Intrinsically weaker M1 (magnetic dipole) transitions are of considerable practical importance in the atmosphere due to the high abundance of O_2. We will see that collision induced E2 (electric quadrupole) absorption involving N_2 and O_2 is measurable in the atmosphere. The different atmospheric hydrometeors (water droplets, snow, graupel, hale, ice cristals,...) scatter and absorb following different patterns across the longwave (radio to submm) spectral region. All the mechanisms involved in the radiative transfer of longwave radiation in the atmosphere will be described in this chapter.

10.1.2 Thermodynamics of the air

Gas mixture: Dalton's law A mixture of ideal gases behaves like an ideal gas:

$$\text{Partial pressures}: \quad p_1 V = \mathcal{N}_1 kT, \quad p_2 V = \mathcal{N}_2 kT, \quad ... \tag{10.1}$$

$$\text{Total pressure}: \quad pV = (p_1 + p_2)V = (\mathcal{N}_1 + \mathcal{N}_2)kT + ... \quad = \mathcal{N} kT \tag{10.2}$$

Dry air is a mixture of N_2, O_2, ... molecules. It behaves indeed very much like an ideal gas: $R_a = c_{p_a} - c_{v_a} = 8.3143$ J/mol-deg (vs 8.3149 for an ideal gas), $\gamma_a = 1.404$ (vs 1.400 for ideal rigid molecules).

Wet air (without clouds) is a mixture of dry air + H_2O molecules. It is customary to denote by e the partial pressure of water vapor, p_a that of dry air, and p' the wet air pressure. The specific heats of water *vapor* are not that different from those of ideal gases: $c_{v_w} = 25.3 + 210^{-3}(T - 273)$; $\gamma_w = 1.37$, vs $c_v = 3R = 24.9$ and $\gamma = \frac{4}{3}$ for a rigid asymmetric top.

Then, Dalton's law yields:

$$c'_v = (1 - \frac{e}{p'})c_{v_a} + \frac{e}{p'}c_{v_w} \simeq (1 + 0.2\frac{e}{p'})c_{v_a} \tag{10.3}$$

The fractional abundance of water vapor and $\frac{e}{p}$ reaching seldom a few percent, the wet air constants are within a small correction term equal to the dry air constants. In particular, introducing the volume density ρ, it is customary to write:

$$p' = \frac{R\rho' T}{M'} = \frac{R\rho T'}{M_a} \tag{10.4}$$

where $T' = \frac{M'T}{M_a} = T(1 - 0.378\frac{e}{p'})^{-1}$, is the *virtual temperature*.

Then, for the adiabatic expansion of a wet air bubble, one has:

$$T' = Cst \times p^{m'} \tag{10.5}$$

m' is equal to m_a within few per mil, so, in practice, the adiabatic curves of dry air can be used for wet air (without clouds), provided one replaces T by T' (the difference could reach a few K and could be important near 0°C). In the following, we drop the 'prime' signs, except for the virtual temperature T'.

10.1.3 Hydrostatic equilibrium

At large scales, the air pressure and density depend essentially on the massive and slowly varying dry component and are well described by *hydrostatic equilibrium*. The air temperature, as we have seen, depends significantly on the abundance and distribution of water, CO_2 (and O_3 for the stratosphere).

At equilibrium:

$$dp/dh = -g\rho \qquad p = \frac{\rho R T'}{M_a} \tag{10.6}$$

where ρ is the density at an altitude h, p is the pressure, $T' \simeq T$ the air "virtual" temperature. $M_a \simeq 29$ is the average molecular weight, and g the local gravitational field.

$$\frac{dp}{p} = \frac{-gM_a}{RT'}dh \tag{10.7}$$

In the "standard atmosphere" model, T', the temperature of the air varies linearly with altitude and is given throughout the troposphere (i.e. between h=0 and 11 km) by: $T' = T'_o - b(h - h_o)$, where b (in $\mathrm{K\,km^{-1}}$) is a constant. Let us first consider a relatively small change in altitude: $h - h_o \leq 1$ km, $T' \simeq T'_{ave} = (T'(h) + T'(h_o))/2$; we find Laplace's hydrostatic formula:

$$\frac{\rho}{\rho_0} \simeq \frac{p}{p_0} \simeq e^{-\frac{gM_a h}{RT'_{ave}}} = e^{-\frac{h}{h_o}} \tag{10.8}$$

where ρ_o is the density at sea level and $h_o = RT/M_a g = 8.4(T/288)$ km, the scale height. The gas column densities (expressed in $\mathrm{g.cm^{-2}}$) along the vertical above sea level (N_o) and above a point at altitude h (N) are:

$$N_o M_a = \int \rho dh = \rho_o h_o \;\; ; \qquad N = N_o e^{-h/h_o} \tag{10.9}$$

For larger altitudes, from Eq.10.7 and $dh = -dT'/b$, then:

$$\frac{dp}{p} = \frac{gM_a}{bR}\frac{dT'}{T'} \;\; ; \qquad \rho = \rho_o(\frac{T'}{T'_o})^{s-1} \tag{10.10}$$

with $s = gM_a/(bR)$.

Although the above equations represent fairly well the density and pressure throughout the troposphere, the temperature distribution can depart significantly from the above linear variation near the ground. This ground heats up faster than the transparent air during the day, and cools off more rapidly during the night. The temperature gradient at low altitudes (up to 1-2 km) can be thus steeper or shallower than described by b ($\mathrm{K\,km^{-1}}$). Occasionally, it can be inverted, the temperature increasing with altitude. The *inversion*

layer usually stops briskly at 1 or 2 km altitude and the normal temperature gradient resumes above. Inversion layers are common during the night over bare land. They can also be caused by hot winds blowing from the sea.

The local temperature gradient determines stability of the air to vertical motions. A rising bubble of wet air expands adiabatically as long as the water vapor it contains does not condense. Expanding, it cools almost as an ideal gas with:

$$T \propto p^m \text{ and } m = (1 - 0.23q)m_a \simeq m_a \tag{10.11}$$

The pressure is set by the surrounding air (Eq.10.8), and the bubble seen to cool down with an "adiabatic" gradient of

$$\frac{dT}{dh} = -g\frac{M_a}{C_p} = 9.8\text{Kkm}^{-1}$$

If the actual temperature gradient is smaller than the adiabatic gradient, the bubble becomes cooler, hence denser than the surrounding air and its ascent stops. The air is stable. If the local gradient is larger than the adiabatic gradient, the bubble becomes less dense than the surrounding air; the air is unstable and a thick convection layer develops, a situation likely to happen in a hot summer afternoon.

10.1.4 Water

The scale height of water, h_w, which results from a fast evaporation/condensation process, is small (typically 2 km) compared to the equilibrium scale height $h_o = 8.4$ km. At $h = 2.5$ km, the altitude of the Plateau de Bure, the water vapor column density N_w (or w, "amount of precipitable water", when expressed in g.cm^{-2}, or cm of water) is normally reduced by a factor of 3-4, with respect to sea level. This factor, as we have seen, is strongly modulated by the local temperature gradient. w is lower in the presence of a low altitude inversion layer which reduces the vertical turbulence and traps most of the water well below the observatory.

10.2 Atmospheric radiative transfer in the mm/submm

Due to space constraints in this book we cannot provide a very detailed overview of all aspects involved in modeling the longwave atmospheric spectrum. The author and co-workers have recently published an in-depth description of their radiative transfer model ATM (Atmospheric Transmission at Microwaves, Pardo et al [2001b]) that can serve as a reference for the information that is missing here. That model has been adopted in this chapter.

10.2.1 Introduction

Accurate modeling of the longwave emission/absorption spectrum of the terrestrial atmosphere is needed in many scientific applications. In the astrophysical domain, it is needed to predict the atmospheric attenuation at a given frequency for ground-based and airborne observatories, to calculate system noise temperatures and to estimate phase delays for interferometry. In remote sensing of the atmosphere and the Earth's surface, obtaining useful data for meteorological and environmental studies relies upon an accurate knowledge of the atmospheric spectrum.

We will see in this chapter how to model the Earth's atmosphere longwave spectrum. For millimeter and submillimeter astronomy applications we need to know for a given path through the atmosphere, the opacity, radiance, phase delay and polarization[1].

10.2.2 Unpolarized radiative transfer equation

The unpolarized radiative transfer in non-scattering media is described by a relatively simple differential scalar equation:

[1] Polarization can be produced by different mechanisms such as emission of paramagnetic molecules such as O_2 under the effect of the geomagnetic field, by radiation scattering by hydrometeors, or by reflection on a Fresnel-like (ocean) surface.

$$\frac{dI_\nu(\vec{r},\vec{n}}{ds} = \epsilon_\nu - \kappa_\nu I_\nu(\vec{r},\vec{n}) \tag{10.12}$$

where I_ν is the radiance (in W m^{-2}ster^{-1}cm^{-1}), $\epsilon_\nu dw d\nu ds d\sigma$ and $\kappa_\nu I(\vec{r},\vec{n},\nu) dw d\nu d\sigma ds$ are the amounts of energy emitted and absorbed at frequency ν in a pencil of solid angle dw in the direction $\vec{r}$ through a cylinder of length ds and cross-section $d\vec{\sigma}$=$d\sigma\vec{n}$. ϵ_ν and κ_ν are the macroscopic absorption and emission coefficients. The absorption coefficient gives the fractional loss of intensity (at a given wavelength) per length through an absorbing medium.

After rearranging equation 10.12 and considering absence of scattering, the radiative transfer problem is unidimensional in the direction of $\vec{r}$. We can formulate it under *Local Thermal Equilibrium* (LTE) conditions as follows:

$$\frac{dI_\nu(s')}{d\tau_\nu} = -I_\nu(s') + S_\nu(T[s']) \tag{10.13}$$

where s' is a coordinate along the path, $S_\nu = \epsilon_\nu/\kappa_\nu$ is the so-called *source function*, and $d\tau_\nu = \kappa_\nu ds$ is the *differential opacity*.

The solution of this equation can be given in an integral form:

$$I_\nu(s) = I_\nu(0)e^{-\tau_\nu(0,s)} + \int_0^s S_\nu(s')e^{-\tau_\nu(s',s)}\kappa_\nu(s')ds' \tag{10.14}$$

In general, the line-by-line integrated opacity corresponding to a path through the terrestrial atmosphere is calculated in a discrete way as follows:

$$\tau_\nu(s',s) = \sum_{i(layers)} [\sum_{j(molec.)} (\sum_{k(resonances)} \kappa_{\nu_k})_j]_i \cdot \Delta s_i \tag{10.15}$$

where Δs_i is the path through the homogeneous i-th layer in the path from s' to s and no line coupling between different species is assumed. As pressure increases the calculations have to use thiner layers to follow the opacity distribution.

The absorption coefficient of an electric dipole (E1) resonance in the atmosphere is given in general by the following equation:

$$(\kappa_\nu)_{lu} = \frac{8\pi^3 N\nu}{3hcQ}(e^{-E_l/KT} - e^{-E_u/KT}) \cdot |< u \mid \mu \mid l >|^2 \, f(\nu,\nu_{l\to u}) \tag{10.16}$$

where N is the number density in the relevant vibrational state the molecule, E_n the energy level of the state and g_n its degeneracy, Q is the partition function, μ is the dipole operator of the transition and $\mid u >$, $\mid l >$ are the wavefunctions of the upper and lower states, and, finally, $f(\nu,\nu_{l\to u})$ is the line shape function. This the basic expression used in the ATM model.

10.2.3 Spectroscopic parameters

Both transition probabilities $|< u \mid \mu \mid l >|^2$ and rotational energy levels (from which both resonance frequencies and population factors under LTE are determined) can be obtained from the rotational hamiltonians. The number of rotational constants depends on the type of molecule. The cases to be considered in the atmosphere are diatomic or linear molecules (with no magnetic moment), symmetric rotors in $^3\Sigma$ electronic state, and asymmetric rotors.

Transition probabilities:

The way we parametrize them is the following:
$|< J,\tau \mid \mu \mid J',\tau' >|^2 = \mu_g^2 \lambda_g(J,\tau,J',\tau')$. J, J' represent rotational quantum numbers, τ, τ' are other quantum numbers, μ_g is the value of the dipole moment (electric or magnetic), and $\lambda_g(J,\tau,J',\tau')$ is a dimensionless parameter called the *oscillator strength* of the particular transition.

Partition function:

The case of symmetric linear or diatomic molecules ($^{16}O_2$, N_2O or CO) and the general asymmetric rotors must be treated individually. In the first case the energy levels are ∼hBJ(J+1) where B is the rotational constant of the molecule in the considered vibrational state. There are corrections to this simple rigid rotor expression but for CO, for example, the associated parameter D is five orders of magnitude smaller than B and for other important atmospheric molecules the ratio B/D is even larger. In the case of asymmetric rotors (O_3, SO_2,...) there are three main rotational constants (A, B, C) in the Hamiltonian related with the three principal axes. There are also corrections due to centrifugal and other effects.

Analytical expressions (see Pardo et al [2001b]) can be used in the atmosphere for both types of molecules within an error not larger than 0.4%.

Spectroscopy of H_2O, O_2, O_3

Of the major molecular constituents of the atmosphere (see Table 10.1) only water vapor and ozone, owing to their bent structure, have a non-zero electric dipole moment. Molecular nitrogen, an homonuclear species, and CO_2, a linear symmetric species, have no permanent electric or magnetic dipole moment in their lowest energy states. These latter molecules, as is the case for most of gaseous molecules, are singlet states, with electrons arranged two-by-two with opposite spins. O_2 has a permanent magnetic dipole owing to two parallel electron spins. It thus presents magnetic dipole transitions of noticeably intensity due to the large abundance of this molecule in the atmosphere.

We present here the details about the spectroscopy of H_2O, O_2 and O_3 because these molecules dominate the longwave atmospheric spectrum as seen from the ground.

Water vapor Water vapor is a C_{2v} molecule (degree of symmetry: σ=2) with a relatively high electric dipole moment: $\mu = 1.88 \cdot 10^{-19}$esu·cm. The first vibrational modes of $H_2^{16}O$ are at 3693.8 cm^{-1} (1,0,0), 1614.5 cm^{-1} (0,1,0) and 3801.7 cm^{-1} (0,0,1). The nuclear spins (1/2 for H, 0 for ^{16}O and ^{18}O, 1/2 for ^{17}O, and 0 for D) lead to two spectroscopically separated species of water: I=1 (statistical weight g=3) [orto-$^{16,18}H_2O$], and I=0 (g=1) [para-$H_2^{16,18}O$]. HDO and $H_2^{17}O$ have a hyperfine structure.

For $^{16,18}H_2O$ each level is denoted, as usual for asymmetric top molecules by three number s $J_{K_{-1},K_{+1}}$. J, which is a "good" quantum number, represents the total angular momentum of the molecule; by analogy with symmetric tops, K_{-1} and K_{+1} stand for the rotational angular momenta around the axis of least and greatest inertia. Allowed radiative transitions obey the selection rules $\Delta J = \pm 1, \Delta K = \pm 1, 3$, with $K_{-1}, K_{+1} : odd, odd \leftrightarrow even, even$ or $o, e \leftrightarrow e, o$. The levels with K_{-1} and K_{+1} of the same parity belong to the *para* species, those of opposite parity belong to *orto* water.

Molecular oxygen Molecular oxygen, although homonuclear, hence with zero electric dipole moment, has a triplet electronic ground state, with two electrons paired with parallel spins. The resulting electronic spin couples efficiently with the magnetic fields caused by the end-over-end rotation of the molecule, yielding a magnetic dipole moment of two Böhr magnetons, $\mu_{mag} = 2\mu_{Böhr} = 1.854 \cdot 10^{-2}$Debyes. The magnetic dipole transitions of O_2 have intrinsic strengths $\sim 10^{2-3}$ times weaker than the water transitions. O_2, however, is 10^{2-3} times more abundant than H_2O, so that the atmospheric lines of the two species have comparable intensities.

The spin of 1 makes of the ground electronic state of O_2 a triplet state ($^3\Sigma$). **N**, the rotational angular momentum couples with **S**, the electronic spin, to give **J** the total angular momentum: $\mathbf{N} + \mathbf{S} = \mathbf{J}$. The **N**·**S** interaction (and the electronic angular momentum–electronic spin interaction **L**·**S**) split each rotational

level of rotational quantum number $N \geq 1$ into three sublevels with total quantum numbers

$$J = N + 1, J = N \quad \text{and} \quad J = N - 1$$

the $J = N+1$ and $J = N-1$ sublevels lying below the $J = N$ sublevel by approximately $119(N+1)/(2N+3)$ GHz and $119/(2N-1)$ GHz, respectively. Note that the two identical ^{16}O nuclei have spins equal to zero and obey the Bose-Einstein statistics; there are only odd N rotational levels in such a molecule.

The magnetic dipole transitions obey the rules $\Delta N = 0, \pm 2$ and $\Delta J = 0, \pm 1$. Transitions within the fine structure sublevels of a rotational level (i.e. $\Delta N = 0$) are thus allowed. The first such transition is the $(J, N) = 1, 1 \leftarrow 0, 1$ transition, which has a frequency of 118.75 GHz. The second, the $1, 1 \leftarrow 2, 1$ transition, has a frequency of 56.26 GHz. It is surrounded by a forest of other fine structure transitions with frequencies ranging from 53 GHz to 66 GHz. The first "true" rotational transition, the $N = 3 \leftarrow 1$ transitions, have frequencies above 368 GHz (368.5, 424.8, and 487.3 GHz). In addition, the permanent magnetic dipole of this molecule can interact with an external magnetic field, leading to a Zeeman splitting of the energy levels. In our atmosphere this splitting is of the order of 1-2 MHz.

The rare isotopomer $^{18}O^{16}O$ is not homonuclear, hence has odd N levels and a non-zero electric dipole moment. This latter, however, is vanishingly small (10^{-5}D).

Ozone The quantum numbers are as in other asymmetric top molecules, such as H_2O. As noted above, ozone is mostly concentrated between 11 and 40 km altitude; it shows large seasonal and, mostly, latitude variation. Because of its high altitude location, its lines are narrow: at 25 km, ρ_a, hence $\Delta\nu$, is reduced by a factor of 20 with respect to see level; moreover, the dipole moment of ozone (μ= 0.53 Debyes), 3.5 times smaller than that of H_2O, further reduces the ozone line widths. Because of their small widths and despite the small ozone abundance, ozone lines have significant peak opacities, especially as frequency increases. This fact can be seen in the high resolution FTS measurements presented in this chapter.

10.2.4 Line shapes

Absorption

In the lower atmospheric layers (up to $\sim$ 50 km, depending on the molecule and the criteria) the collisional broadening mechanism (also called pressure-broadening) dominates the line shape. One approximation to the problem considers that the time between collisions, τ_{col} ($\propto p^{-1}$), is much shorter than the time for spontaneous emission, τ_{rad}, which is, in the case of a two level system, $1/A_{u\to l}$ where $A_{u\to l}$ is the Einstein's coefficient for spontaneous emission. This approximation leads to the so-called Van Vleck & Weisskopf profile, normalized as follows to be included in equation 10.16:

$$f_{VVW}(\nu, \nu_{l\to u}) = \frac{\nu\Delta\nu}{\pi\nu_{l\to u}}\left(\frac{1}{(\Delta\nu)^2 + (\nu - \nu_{l\to u})^2} + \frac{1}{(\Delta\nu)^2 + (\nu + \nu_{l\to u})^2}\right) \tag{10.17}$$

where $\Delta\nu$ is the collision broadening parameter.

This lineshape describes quite well the resonant absorption in the lower atmospheric layers except for very large shifts from the line centers. For example, all the mm/submm resonances of H_2O and other molecules up to 1.2 THz are well reproduced using this approximation within that frequency range. Some properties of the collision broadening parameters in the atmosphere are:

$$\Delta\nu(p, T) = \Delta\nu(p_0, T_0)\frac{p}{p_0}\left(\frac{T_0}{T}\right)^{\gamma} \tag{10.18}$$

$$\Delta\nu(M - dry\ air) = X_{N_2}\Delta\nu(M - N_2) + X_{O_2}\Delta\nu(M - O_2) \tag{10.19}$$

where X are the volume mixing ratios. Laboratory measurements for individual lines are the only source of precise information about the parameters γ and $\Delta\nu(M - N_2, O_2)$ for the different atmospheric trace

gases M. The exponent γ has been found in most cases to be in the range 0.6 and 1.0. For O_2 and H_2O self-collisions have to be considered.

When the pressure gets very low the Doppler effect due to the random thermal molecular motion dominates the line broadening:

$$\mathcal{F}_D(\nu, \nu_{l\to u}) = \frac{1}{\Delta\nu_D}(\frac{\ln 2}{\pi})^{1/2} exp[-(\frac{\nu - \nu_{l\to u}}{\Delta\nu_D})^2 \ln 2] \tag{10.20}$$

where the halfwidth parameter is given by:

$$\Delta\nu_D = \frac{\nu_{l\to u}}{c}\sqrt{\frac{2\ln 2kT}{m}} = 3.58 \cdot 10^{-7}\nu_{l\to u}\sqrt{\frac{T}{M}} \tag{10.21}$$

M being the molecular weight of the species in g/mol.

If the collisional and thermal broadening mechanisms are comparable the resulting line-shape is the convolution of a Lorentzian (collisional line shape at low pressures) with a Gaussian: a Voigt profile.

Phase delay

Besides absorption, the propagation through the atmosphere also introduces a phase delay. This phase delay increases as the wavelength approaches a molecular resonance, with a sign change across the resonance. The process can be understood as a forward scattering by the molecular medium in which the phase of the radiation changes.

Both the absorption coefficient and the phase delay can be treated in a unified way for any system since both parameters are derived from a more fundamental property, the complex dielectric constant, by means of the Kramers-Krönig relations. A generalized (complex) expression of the VVW profile, which accounts for both the Kramers-Krönig dispersion theory as well as line overlapping effects (parameter δ) is the following ($\nu_{l\to u} \equiv \nu_{lu}$):

$$\mathcal{F}_{VVW}(\nu, \nu_{lu}) = \frac{\nu}{\pi\nu_{lu}}[\frac{1 - i\delta}{\nu_{lu} - \nu - i\Delta\nu} + \frac{1 + i\delta}{\nu_{lu} + \nu + i\Delta\nu}] \tag{10.22}$$

the imaginary part of which reduces to equation 10.17 when δ=0.

10.2.5 Non-resonant absorption

H_2O pseudocontinuum

Lines with resonant frequencies up to a given frequency (10 THz in our case) are included in line-by-line calculations. Since the true lineshape is not known accurately beyond a few times the halfwidth from the line centers (this may be due to the finite collision time, the complexity of the calculations and the lack of precise laboratory data), a broadband "continuum"-like absorption term needs to be included for accurate results in the longwave domain.

Dry continuum-like absorption

The non resonant absorption of the dry atmosphere is made up of two components: collision induced absorption due to transient electric dipole moments generated in binary interactions of symmetric molecules with electric quadrupole moments such as N_2 and O_2, and the relaxation (Debye) absorption of O_2.

Pseudocontinua in ATM

In the ATM model model, we introduce collisionally-induced dry absorption and longwave (foreign) pseudocontinuum water vapor absorption derived from our previous FTS measurements performed on top of

Mauna Kea, Hawaii. For both terms we use ν^2 frequency power laws, with the coefficients as determined by Pardo et al [2001a].

$$\kappa_{c,H_2O} = 0.031 \cdot \left(\frac{\nu}{225}\right)^2 \cdot \left[\frac{e}{1013} \cdot \frac{p-e}{1013}\right] \cdot \left(\frac{300}{T}\right)^3 \quad m^{-1} \tag{10.23}$$

$$\kappa_{c,dry} = 0.0114\left(\frac{p-e}{1013}\right)^2\left(\frac{300}{T}\right)^{3.5}\left(\frac{\nu}{225}\right)^2 \quad m^{-1} \tag{10.24}$$

The validity of these expressions is restricted to frequencies $\leq$1.1 THz (the upper limit of our current data), although there are indications that they can be extended to 2 THz with no important loss of accuracy.

10.2.6 Radiative transfer through atmospheric hydrometeors

The equation describing the transfer of radiation through an atmosphere that contains scatterers is as follows:

$$\mu\frac{dI(z,\mu)}{dz} = K(z,\mu)I(z,\mu) - 2\pi\int_{-1}^{1} M(z,\mu,\mu')I(z,\mu')d\mu' - \sigma(z,\mu)B[T(z)] \tag{10.25}$$

where:
• I=(I,Q,U,V)^T is the Stokes vector describing the propagating electromagnetic field.
• K is the extinction matrix.
• M is the zeroth Fourier component of the phase matrix.
• σ is the emission vector.
• $B(T)$ is the blackbody spectrum at temperature T.
• μ=cos(θ) (θ=zenith angle, 0⇒downwards). The frequency dependence in several of these quantities is implicit. Finally, z is the vertical coordinate in a plane-parallel atmosphere.

K, M and σ are related according to:

$$K(\mu) = 2\pi\int_{-1}^{+1} M(z,\mu,\mu')d\mu' + \sigma(\mu) \tag{10.26}$$

which is a consequence of the detailed energy balance.

The frequency independent (excluding Raman effect or fluorescence) far-field scattering by single non-spherical particles has been incorporated to the ATM model. It is computed using state-of-the-art T-Matrix routines developed by Mishchenko [2000]. For the integration over all possible orientations to be possible, it is necessary to be in the single scattering regime. Then, each particle is in the far-field zone of the others. This implies that the average distance between particle centers is larger than 4 times their radii. This requirement is usually satisfied by cloud and precipitation particles. The scattered fields are then incoherent and their Stokes parameters can simply be added.

For estimates concerning the effect of clouds to ground-based observations a plane parallel geometry is assumed, as a first approach, with thermal emission as the only source of radiation. The hydrometeors can be either totally randomly-oriented or at least azimuthally randomly oriented. In both cases, the radiation field is azimuthally symmetric leading the Stokes parameters U and V to vanish so that the dimension of tensorial equation (10.25) reduces to be 2. This radiative transfer equation can then be integrated using the quite standard method called *doubling and adding*, introduced in the ATM model according to Evans & Stephens [1991].

To illustrate the effect of two different types of clouds, we have performed first a simulation where we add to a clear atmosphere containing 1 mm of water vapor a layer between 6 and 6.5 km that contains spherical water droplets with a radius of 40 μm and a liquid water path of 0.1 km/m^2. The second simulation replaces the water droplets for spherical ice particles with a radius of 100 μm. The effect of liquid water is quite large since it is a quite effective absorber. The effect of ice is much more related with its scattering properties and becomes more important at shorter wavelengths.

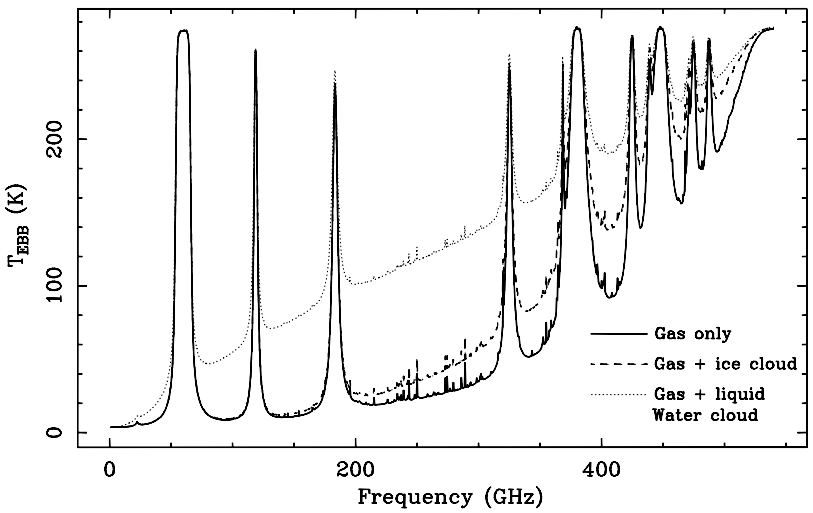

Figure 10.1: Simulations of the effect of clouds in the brightness temperature of the atmosphere at zenith. The liquid water and ice layers have been placed between 6.0 and 6.5 km, the equivalent water path is 0.1 km/m^2 for both but the size of the spherical particles is 40 μm for liquid water and 100 μm for ice. The considered atmosphere contains 1 mm of water vapor column.

10.3 Fourier Transform Spectroscopy for site testing

10.3.1 FTS measurements at Mauna Kea

Broadband submillimeter atmospheric measurements with a Fourier-transform spectrometer have been performed in recent years at the Caltech Submillimeter Observatory (CSO) with the primary goal of accurately measuring the atmospheric transmission in the submillimeter-wave domain and using the data to build a state-of-the-art transmission model.

The instrument used for this work has been described in Serabyn & Weisstein [1995]. Recently, new 1.1 THz and 1.6 THz low-pass filters have been installed in front of the ^{3}He cooled bolometer detector in order to efficiently cover both the full subTHz domain and the supraterahertz windows that are predicted by theory. The first successful measurements on Mauna Kea using the 1.1 THz filter were obtained on the night of 1998 April 1^{st} under extremely dry "El Niño" conditions. It was estimated that the H_2O column was under 0.2 mm, so it is clear that these data offered the best opportunity for a determination of the dry and wet longwave nonresonant terms [$\kappa_{c,dry}(\nu)$, $\kappa_{c,H_2O}(\nu)$]. However, to separate one from the other, an independent measurement under the same P/T conditions was needed. This occurred in a second run in July 1999, greatly simplifying our analysis (see Figure 10.2). From these 2 datasets, our goals have been to:

I) Extract the dry continuum from our measurements and determine its origin.

II) Determine the H_2O excess absorption in the submillimeter domain in low humidity conditions (when only foreign-gas collisions have to be taken into account), and compare it to proposed formulations.

The separation of these two terms using the data from the upper panel of Figure 10.2 is described in detail in Pardo et al [2001a] and leads to the formulation given in section 10.2.5. This is the first time that such a separation is done successfully in the submillimeter.

Our results indicate that the H_2O and dry continuum-like terms of existing models are not accurate in the submillimeter range and that the models should be updated accordingly. This has been done in Pardo et al [2001b]. The lower panel of Figure 10.5 shows the April 98 data and the separate opacity contributions that add up to fit the observed opacity.

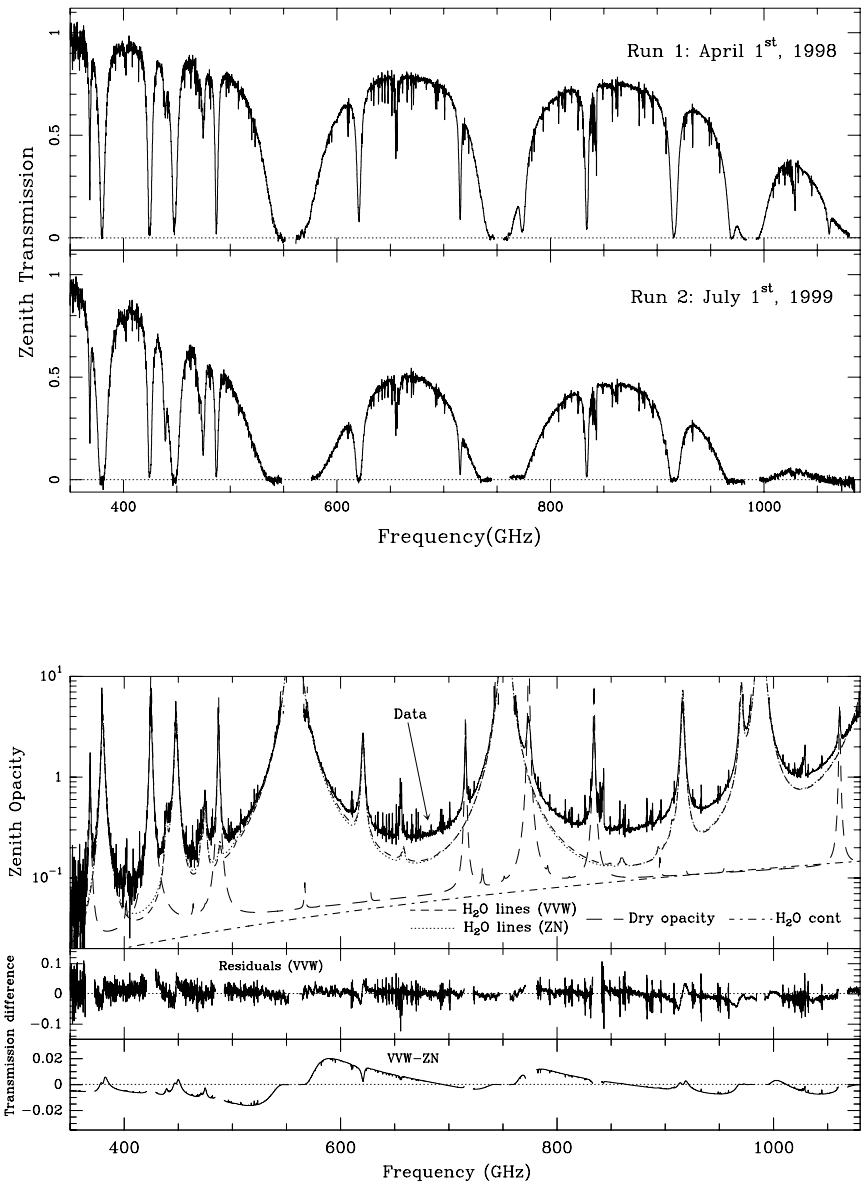

Figure 10.2: Upper panel: High resolution fully calibrated FTS atmospheric zenith spectra ($\Delta\nu$=199 MHz) obtained with the FTS experiment at Mauna Kea (Hawaii). Bottom Panel: Fit of the above April 98 zenith spectrum, shown in terms of opacity on a logarithmic scale. The opacity contributions from the different species and the continua leading to the final fit are plotted separately (assuming a VVW line shape for water). The middle panel shows the fit residual when using a VVW lineshape. The bottom panel is the difference between the fit considering VVW lineshapes and the one considering Zhevakin-Naumov (ZN) profiles.

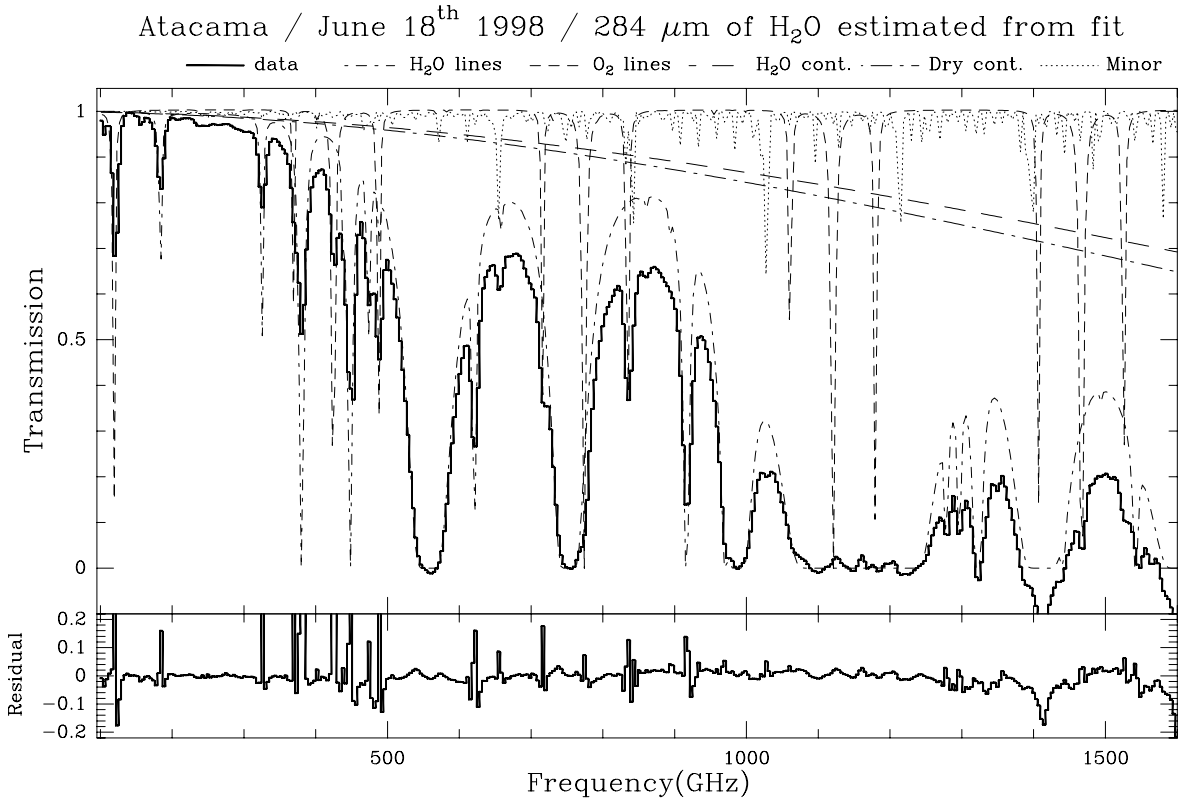

Figure 10.3: Atmospheric transmission spectrum obtained at Pampa La Bola on 1998 June 17 (courtesy of Satoki Matsushita). The absorption line and continuum components from the ATM fit of the data, along with the fit residual are also shown.

10.3.2 FTS measurements at Atacama (future ALMA site)

Two other FTS experiments are reported at sites in the Atacama desert, undergoing site testing measurements in areas selected for the Atacama Large Millimeter Array (ALMA) construction.

The first of such experiments has been operated by Nobeyama Observatory at Pampa la Bola, 4800 m above sea level in northern Chile on September 1997 and June 1998. The instrument is a Martin-Puplett type FTS with an InSb bolometer as detector. The frequency range covered is 150 – 1600 GHz (or 2 mm to slightly under 200 μm wavelength). Further details on the instrument can be found in Matsushita et al [1999].

On the morning of 1998 June 17, the best atmospheric transmission spectrum of the experiment was recorded. (Fig. 10.3, *top*). However, due to the limited sensitivity around 1500 GHz and offset errors in the phase correction of the Fourier-transformed spectra, there are some systematic errors in the transmission spectra around the 1450 – 1600 GHz window (it could be up to 10% in transmission). During the observing run, side-by-side measurements with the second FTS experiment in the area (at Chajnantor [Paine et al 2000]) were performed. The measured transmission spectra showed very good correspondence to each other within an accuracy of $\leq 1\%$ in the 650 GHz and 850 GHz windows.

Again, radiative-transfer calculations using the model ATM were performed to fit the data. The best fit of the June 17^{th} spectrum is shown in Fig. 10.3. The model, that took advantage of what we learned from the Mauna Kea data, fits very well the observed spectrum with only one free parameter (the precipitable water vapor column $[N_{H_2O}]$ above the site) except for frequencies higher than 1350 GHz, where the measurement suffers from systematic errors. The fit results in a water vapor column of 0.284 mm.

10.4 Atmospheric absorption evaluation

Calculations of zenith atmosphere opacity at 2.5 and 2.9 km, the altitude of the IRAM sites, can be performed with the updated ATM model [Pardo et al. 2001b] (see Figure 10.4). In fact, the model itself has been installed on-line on the IRAM telescopes of Pico Veleta and Plateau de Bure; it is activated at each calibration or skydip and allows to interpret the observed sky emissivity in terms of water and oxygen contributions and of upper and lower sideband opacities. Note that the opacities derived from sky emissivity observations do not always agree with those calculated from the measurement of P, T, and the relative humidity on the site, as water vapor is not at hydrostatic equilibrium.

The typical zenith atmospheric opacities, in the dips of the 1.3 mm and 0.8 mm windows (e.g. at the frequencies of the $J = 2 - 1$ and $3 - 2$ rotational transitions of CO, 230.54 and 345.80 GHz), are respectively 0.15–0.2 and 0.5–0.7 in winter at the IRAM sites. The astronomical signals at these frequencies are attenuated by factors of respectively $\simeq$ 1.2 and 2 at zenith, 1.3 and 2.8 at 45 degree elevation, and 1.7 and 6 at 20 degree elevation. Larger attenuations are the rule in summer and in winter by less favorable conditions. The $J = 1 - 0$ line of CO, at 115.27 GHz, is close to the 118.75 GHz oxygen line. Although this latter is relatively narrow, it raises by $\simeq$0.3 the atmosphere opacity (which is 0.35–0.4). The atmosphere attenuation is then intermediate between those at 230 and 345 GHz (by dry weather, however, it is more stable than the latter, since the water contribution is small). The measurement of accurate CO line intensity ratios (even not considering the problems linked to differences in beam size and receiver sideband gain ratios) requires therefore good weather, a high source elevation, and a careful monitoring of the atmosphere.

During the past few years, new ground-based astronomical observatories have been built to allow access to the submillimeter range of the electromagnetic spectrum. Potential sites are now being tested for more ambitious instruments such as the *Atacama Large Millimeter Array* (ALMA). All of these are remote, high altitude sites. For our simulations we have selected three sites of interest for submillimeter astronomy: Mauna Kea, HI, USA (LAT=19:46:36, LONG=-155:28:18; home of the Caltech Submillimeter Observatory, James Clerk Maxwell Telescope and Submillimeter Array), Chajnantor, Chile (LAT=-23:06, LONG=-67:27; site selected for ALMA) and the Geographic South Pole (site of the Antarctic Submillimeter Telescope and Remote Observatory). The results of this comparison are also shown on Figure 10.4.

10.4.1 Correction for atmospheric absorption, T_A^*

By analogy with the Rayleigh-Jeans approximation, $I = 2kT/\lambda^2$, which strictly applies to long wavelengths, the mm-wave radio astronomers have introduced the concept of "radiation" or "effective" temperatures, which scale *linearly* with the detected power.

The noise power detected by the telescope is the sum of the power received by the antenna, $\mathcal{W}_A$, and of the noise generated by the receiver and transmission lines, $\mathcal{W}_{rec}$.

Using Nyquist's relation $\mathcal{W} = kT\Delta\nu$, $\mathcal{W}_A$ and $\mathcal{W}_{rec}$ can be expressed in terms of the temperatures T_A and T_{rec} of two resistors, located at the end of the transmission line, which would yield noise powers equal to $\mathcal{W}_A$ and $\mathcal{W}_{rec}$, respectively: $\mathcal{W}_A + \mathcal{W}_{rec} = kT_A\Delta\nu + kT_{rec}\Delta\nu = k(T_A + T_{rec})\Delta\nu$.

T_A is called the "antenna temperature" and T_{rec} the "receiver temperature". T_A becomes T_{load} when the receiver horn sees a load, instead of the antenna, and T_{gr} when it sees the ground. It should be noted that T_{load} and T_{gr} are not *stricto sensus* equal to the load and ground physical temperatures, but are only "Rayleigh-Jeans" equivalent of these temperatures (they are proportional to the radiated power). For ambient loads, they approach closely the physical temperature, since $h\nu/k \simeq 11$ K at $\lambda = 1.3$ mm.

When observing with the antenna a source and an adjacent emission-free reference field, one sees a change $\Delta T_A = T_A(sou) - T_A(ref)$ in antenna temperature. Because of the calibration method explained below, it is customary, in mm-wave astronomy, to replace ΔT_A, the source antenna temperature, by ΔT_A^*, the source antenna temperature corrected for atmosphere absorption and spillover losses. Both are related through: $T_A = (1 - \eta_f)T_{gr} + \eta_f(T_{sky} + \Delta T_A^* e^{-\tau})$, where τ is the line-of-sight atmosphere opacity. η_f is the forward efficiency factor, which denotes the fraction of the power radiated by the antenna on the sky (typically of the order of 0.9, see also Chapter 1).

The source equivalent "radiation temperature" T_R (often improperly called "brightness temperature" and therefore denoted T_{MB} when it is averaged over the main beam) and ΔT_A^* are related through

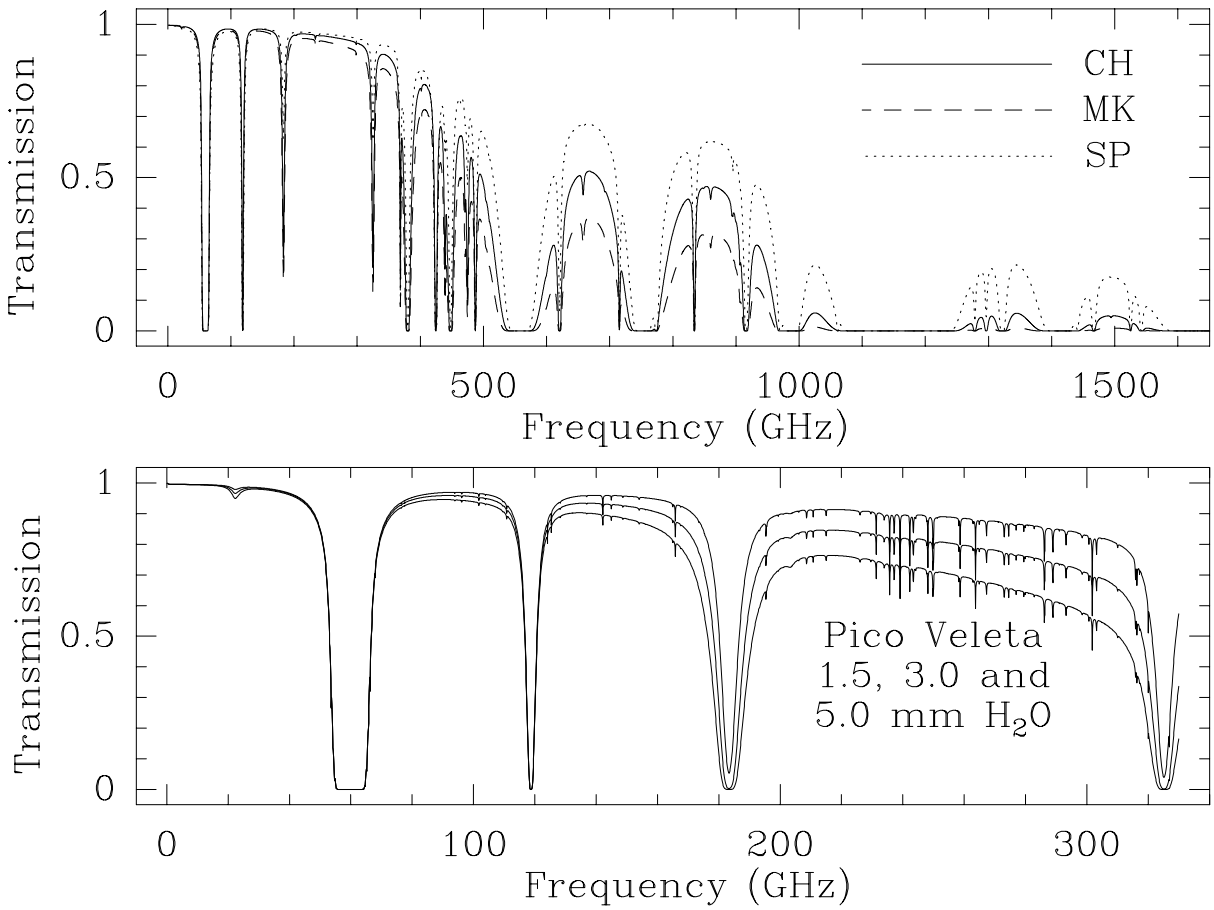

Figure 10.4: Calculated zenith atmospheric transmissions and continuum-like opacities for Mauna Kea, Chajnantor and the South Pole corresponding to the 1^{st} quartile of the cumulative water column statistics for winter time in the three sites. The H_2O cumulative distributions used here were derived from different methods leading probably to a comparative optimistic result for the South Pole. For comparison we have added the expected transmission in the millimeter range for Pico Veleta in winter for 1.5, 3.0 and 5.0 mm of water vapor.

$$\Delta T_A^* = \int_{sour} T_R \mathcal{A}(x,y) dx dy$$

where $\mathcal{A}(x,y)$ is the antenna power pattern. For a source smaller than the main beam, $\Delta T_A^* = \eta_b/\eta_f T_{MB}$ (where η_b is the beam efficiency factor, see also Chapter 1).

When observing a small astronomical source with temperature $\Delta T_R >> T_{BG} = 2.7$ K, located at an elevation el, one detects a signal $\mathcal{V}_{sour}$ (of scale: $\mathcal{G}$ volt or counts per Kelvin):

$$\frac{\mathcal{V}_{sour}}{\mathcal{G}} = M_{sour} = T_{rec} + (1-\eta_f)T_{gr} + \eta_f T_{sky} + \eta_b T_{MB} \times e^{-\tau} \tag{10.27}$$

This signal can be compared with the signals observed on the blank sky (T_{atm}), close to the source, and to that observed on a hot load (T_{load}):

$$M_{atm} = T_{rec} + (1-\eta_f)T_{gr} + \eta_f T_{sky}; \quad T_{sky} = (1-e^{-\tau})T_{atm}; \quad M_{load} = T_{rec} + T_{load} \tag{10.28}$$

here, we have neglected the cosmic background and assume, in a first step, that the receiver is tuned single sideband.

Simplest case

(e.g. [Penzias & Burrus 1973])

Let's assume that $T_{load} \simeq T_{gr} \simeq T_{atm}$; then:

$$\begin{aligned} M_{load} - M_{atm} &= \eta_f T_{gr} e^{-\tau} \\ M_{sour} - M_{atm} &= \Delta T_A^* e^{-\tau} \\ \Delta T_A^* &= \frac{M_{sour} - M_{atm}}{M_{load} - M_{atm}} \eta_f T_{gr} \end{aligned} \tag{10.29}$$

Note that in Eq.10.29, the measurement of the antenna temperature includes the atmospheric opacity correction, but does not depend explicitly on an assumption on the atmospheric opacity. We can write:

$$\Delta T_A^* = \frac{M_{sour} - M_{atm}}{M_{load} - M_{atm}} T_{cal} \tag{10.30}$$

where we define T_{cal} as $T_{cal} = \eta_f T_{gr} \simeq \eta_f T_{atm}$.

More realistic case

Typically, the mean atmosphere temperature is lower than the ambient temperature near the ground by about 40 K: $T_{atm} \simeq T_{gr} - 40$ K; then, the formula above still holds if we replace T_{cal} by:

$$T_{cal} = (T_{load} - T_{emi}) e^{\tau} \tag{10.31}$$

$$\begin{aligned} \text{with } T_{emi} &= T_{sky}\eta_f + (1-\eta_f) T_{gr} \\ &= \frac{(T_{load} + T_{rec}) \times M_{atm}}{M_{load}} - T_{rec} \end{aligned} \tag{10.32}$$

$$T_{sky} = (1 - e^{-\tau})(T_{gr} - 40)$$

T_{rec}, the receiver effective temperature is usually calculated by the Y factor method using a cold load (usually cooled in liquid nitrogen, i.e. at 77 K) and an ambient load (e.g. at 290 K).

$$Y = \frac{M_{hot_load}}{M_{cold_load}} \qquad T_{rec} = \frac{T_{hot_load} - Y T_{cold_load}}{Y - 1} \tag{10.33}$$

General case

The receiver is not purely single-sideband. Let us denote by G^l and G^u the normalized gains in the receiver lower and upper sidebands, $G^l + G^u = 1$. The atmosphere opacity per km varies with altitude as does the air temperature.

Then, the above expressions of T_{sky} and T_{emi} should be explicited for each sideband ($j = u$ or l):

$$T_{sky}^j = (1 - e^{-\tau^j}) T_{atm}^j \tag{10.34}$$

$$T_{emi} = T_{sky}^l \eta_f G^l + T_{sky}^u \eta_f G^u + (1 - \eta_f) T_{gr} \tag{10.35}$$

The atmospheric transmission model ATM allows to calculate iteratively τ_ν from a load+ sky measurement. The values of τ^l, τ^u are calculated for the Standard US atmosphere (parameters are: Winter-, Spring-, or Summer-temperature T, altitude, latitude, water vapor w) by summing up the contributions of O_2, H_2O and O_3 (including rare isotopes and vibrationally excited states). A first guess of the amount of precipitable water is made from the ambient temperature, pressure and humidity. Then, the expected T_{sky} and T_{emi} are calculated from the two expressions above and T_{emi} is compared to its value measured from the the observation of the atmosphere and the load (Eq.10.32). The value of w is changed and the calculation of τ^j, T_{sky}^j and T_{emi} restarted. Normally, the process converges after 2 to 4 iterations. Once w and T_{emi} are known, the calibration factor T_{cal} can be derived

$$T_{cal}^j = (T_{load} - T_{emi}) e^{\tau^j} \tag{10.36}$$

and the data calibrated in the T_A^* scale using Eq.10.30.

10.5 Phase fluctuation evaluation

10.5.1 Cause of Phase Fluctuations

The phase measured by an interferometer is the difference in the arrival times of the signals at the different antennas. The phase difference contains useful information about the location and structure of the source, but is also affected by atmospheric inhomogeneities. The complex dielectric constant fluctuates in time and in space as the distributions of water droplets, ice particles, and atmospheric gases suffer variations. In the case of clear atmosphere (no scatterers present) the main source of phase delay is water vapor. When there is more water vapor along the optical path of one of the telescopes, the incoming radiation will experience an additional delay and the measured phase will increase by $\Delta\phi$. With wind the amount of water vapor in the beam of each telescope will change over time and so will the detected phase. This phase delay has a resonant behavior as seen in section 10.2.4. As a result, the source appears to move around in the sky and, if the signals are integrated over a period of time which is long compared to the time scale of the fluctuations (few to tens of seconds), resolution as well as signal strength will be degraded. Fluctuations in the dry component of the atmosphere can also originate phase delays but these are in general less important.

10.5.2 Simulations of phase fluctuations

Present day radio interferometers are mostly limited to frequencies below 350 GHz. Phase delay increases in importance as the frequency increases into the submillimeter domain because of the strength of the atmospheric lines involved in both absorption and dispersion. Using the complex line shape of equation 10.22 we have calculated the derivative of the phase delay respect to the water vapor column $\frac{\partial\phi}{\partial N_{H_2O}}$ (this derivative will be called the *differential phase* and is provided in deg/μm here). The differential phase as a function of frequency has been plotted for the Chajnantor site in Figure 10.5 (where the curve is restricted to those frequencies where the transmission is above 10% when the precipitable water vapor column is 0.3 mm, i.e. very good conditions for single-dish submillimeter observations). Another useful quantity plotted in the same figure is the derivate of the phase delay with respect to the sky brightness temperature ($T_{B,sky}$), since this function relates the phase correction between two antennas to a measurable physical parameter ($T_{B,sky}$). Note however that whereas the differential phase described above depends only on ΔN_{H_2O}, this new quantity depends on N_{H_2O} as well. The curve plotted here corresponds to $\frac{\partial\phi}{\partial T_b}(\nu)$ at N_{H_2O}=0.3mm.

As seen in Figure 10.5, the differential phase becomes much more important in the submillimeter domain than it is at millimeter wavelengths, so its correct estimation and the selection of the best means of monitoring water vapor column differences between different antennas are essential for the success of ground-based submillimeter interferometry. For example, the differential phase is 0.0339 deg/μm at 230 GHz whereas it is -0.4665 and 0.2597 deg/μm at 650 and 850 GHz respectively, roughly an order of magnitude larger.

10.5.3 Phase Correction Methods

There are basically two different phase correction methods:

A) The phase offset due to the atmosphere can be measured *directly* by observing a calibrator, i.e., a strong point source whose position and hence theoretical phase are well known. Assuming instrumental errors are small the difference between the measured and the theoretical phase gives the phase offset introduced by the atmosphere. The phase offsets, which are interpolated between measurements on the calibrator, are subtracted from the measured phase of an astronomical source.

B) The correction can be determined indirectly by detecting the emission from water molecules and calculating the phase error from the differences in the amounts of water along the paths to the individual antennas using a model as presented on Figure 10.5. There are two different approaches to determine the amount of water vapor: (i) *Total Power Method*, where the astronomical receivers measure the continuum emission; and (ii) *Radiometric Phase Correction*, where the emission from water lines is measured by dedicated instruments. So far, radiometers monitoring the 22 GHz and the 183 GHz lines have been built

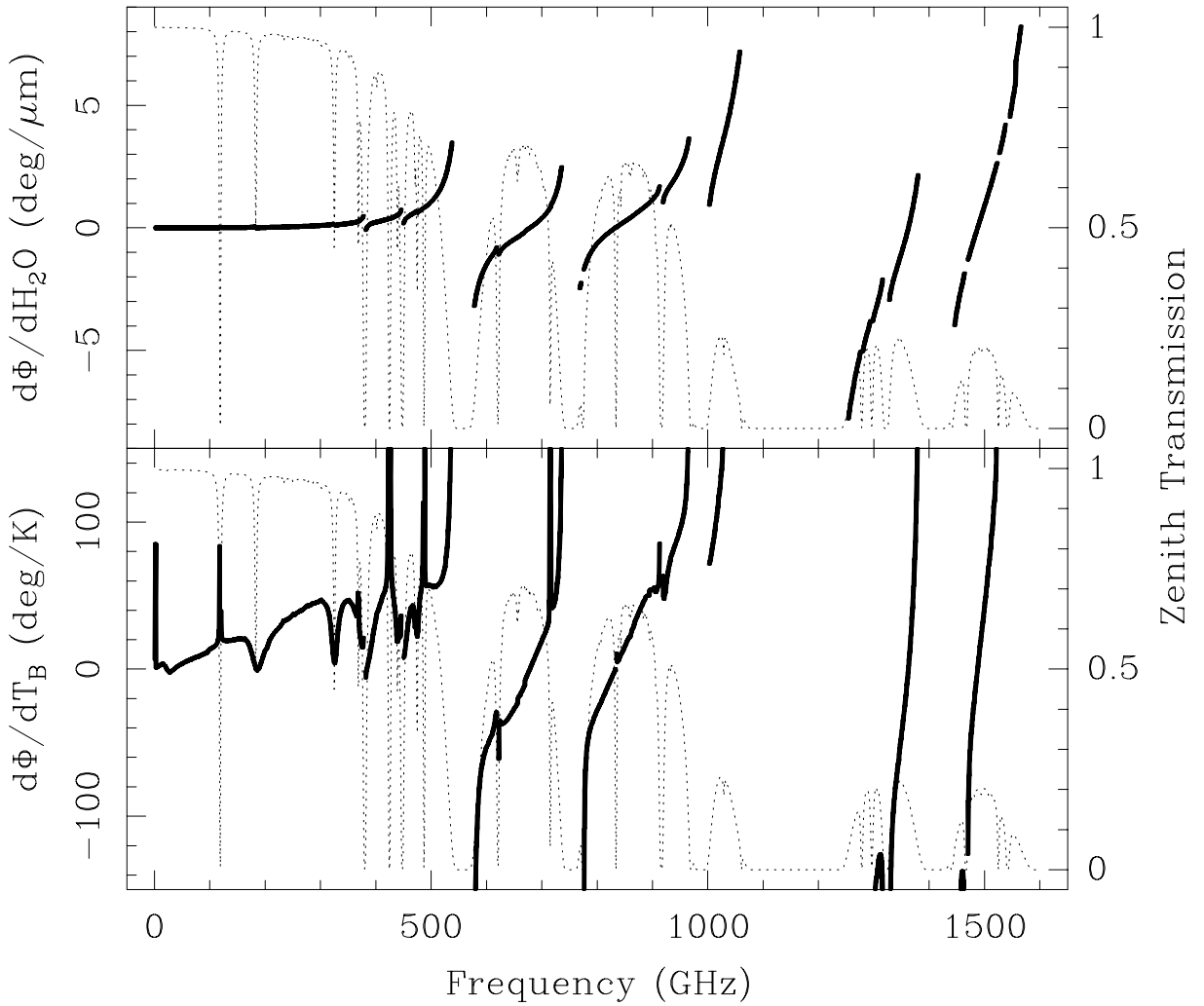

Figure 10.5: Upper panel: Derivative of the phase delay respect to the water vapor column (*differential phase* in text; this derivative is independent of the water vapor column) as a function of frequency, superposed on the Chajnantor atmospheric transmission curve for 0.3 mm of water vapor. Lower panel: Derivative of the phase delay respect to the sky brightness temperature for 0.3 mm H_2O column.

and tested. Receivers at 22 GHz typically have lower noise temperatures than those at 183 GHz, but on (very) dry sites, such as Chajnantor, the 183 GHz monitors will be ideal to measure the optical path with higher accuracy due to the much higher conversion factors from sky brightness temperature in K to optical path length in mm.

10.5.4 Example of phase correction

Fig. 10.6 shows typical phase correction results in normal night time weather for Mauna Kea (2.2 mm N_{H_2O}): The CSO-JCMT interferometer observed bright hydrogen recombination line maser emission towards the source MWC349 at 354 GHz. The solid curve in the top plot displays the measured phase after Doppler correction, it represents the atmospheric phase fluctuations and some electronic phase noise. The dashed line shows the phase predicted by the water vapor monitors. The measured and the predicted phase agree well and their difference is plotted in the lower graph. Phase correction reduces the rms phase fluctuations from 60° (140 μm) to 26° (60 μm) over 30 minutes. If one would integrate on source for 30 minutes 42% of the astronomical flux would be lost due to decorrelation, but with phase correction the

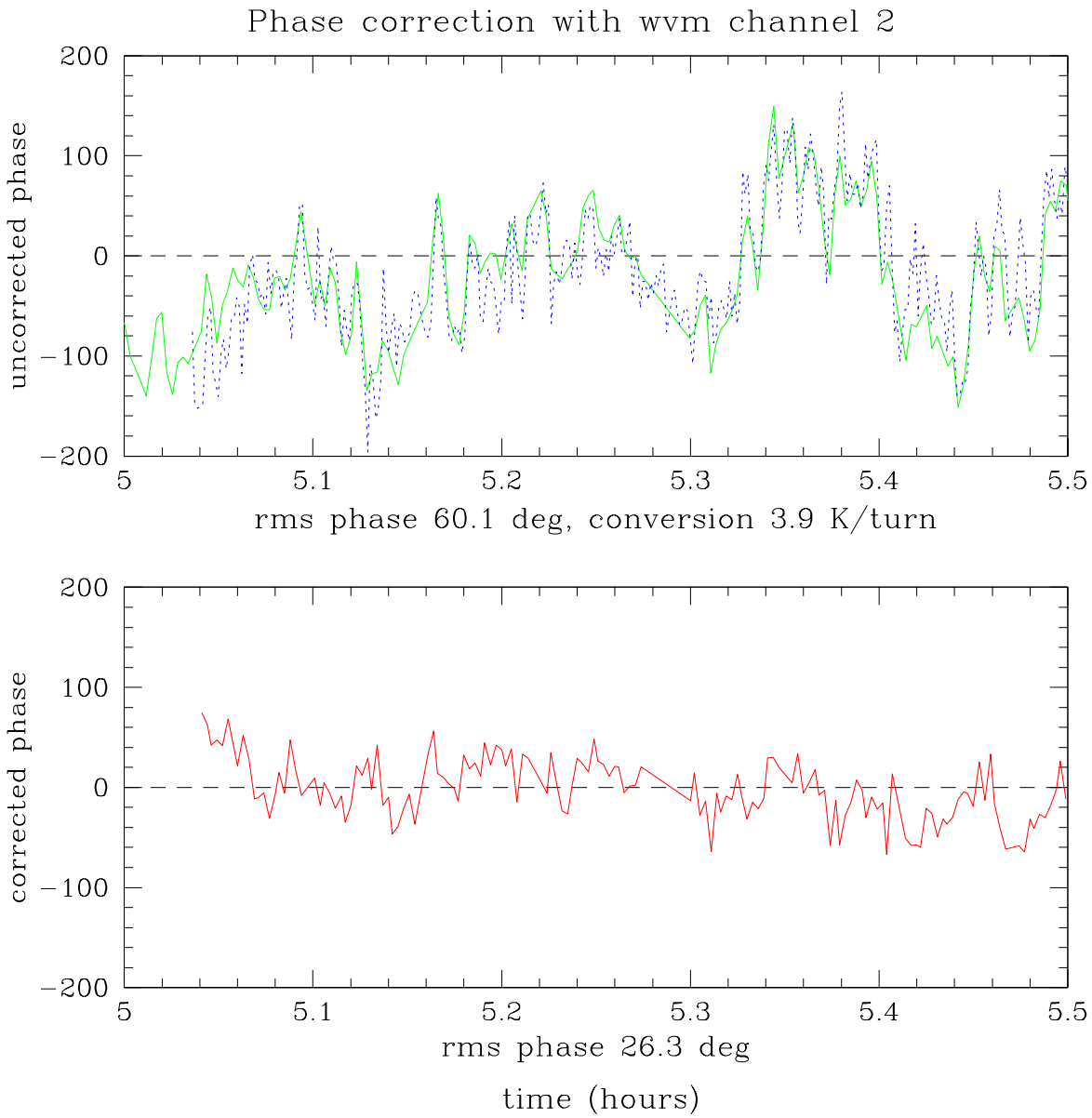

Figure 10.6: Phase correction results for the CSO-JCMT interferometer using 183.31 GHz 3-channel water vapor monitors (courtesy of Martina Wiedner).

loss would amount to only 10%.